Draft version January 25, 2022
Typeset using LaTeX **twocolumn** style in AASTeX63

arXiv:2002.11132v3 [physics.space-ph] 21 Aug 2020

Electron Heating in Perpendicular Low-Beta Shocks

Aaron Tran[1] and Lorenzo Sironi[1]

[1] *Department of Astronomy, Columbia University*
550 W 120th St. MC 5246, New York, NY 10027, USA

ABSTRACT

Collisionless shocks heat electrons in the solar wind, interstellar blast waves, and hot gas permeating galaxy clusters. How much shock heating goes to electrons instead of ions, and what plasma physics controls electron heating? We simulate 2-D perpendicular shocks with a fully kinetic particle-in-cell code. For magnetosonic Mach number $\mathcal{M}_{\rm ms} \sim$ 1–10 and plasma beta $\beta_{\rm p} \lesssim 4$, the post-shock electron/ion temperature ratio $T_{\rm e}/T_{\rm i}$ decreases from 1 to 0.1 with increasing $\mathcal{M}_{\rm ms}$. In a representative $\mathcal{M}_{\rm ms} = 3.1$, $\beta_{\rm p} = 0.25$ shock, electrons heat above adiabatic compression in two steps: ion-scale $E_\parallel = \boldsymbol{E}\cdot\hat{\boldsymbol{b}}$ accelerates electrons into streams along $\boldsymbol{B}$, which then relax via two-stream-like instability. The $\boldsymbol{B}$-parallel heating is mostly induced by waves; $\boldsymbol{B}$-perpendicular heating is mostly adiabatic compression by quasi-static fields.

Keywords: Plasma astrophysics (1261), Space plasmas (1544), Planetary bow shocks (1246), Shocks (2086)

1. INTRODUCTION

Electron heating in collisionless shocks – stated as post-shock electron/ion temperature ratio $T_{\rm e}/T_{\rm i}$ – is not constrained by magnetohydrodynamic (MHD) shock jump conditions. How much do electrons heat, and how do they heat? A prediction for $T_{\rm e}/T_{\rm i}$ can constrain models for gas accretion onto galaxy clusters (Avestruz et al. 2015), and cosmic ray acceleration in supernova remnants (Helder et al. 2010; Yamaguchi et al. 2014; Hovey et al. 2018). Detailed study of the electron heating physics can also help us interpret new high-resolution data from the Magnetospheric Multiscale Mission (Chen et al. 2018; Goodrich et al. 2018; Cohen et al. 2019).

In the heliosphere, shocks of magnetosonic Mach number $\mathcal{M}_{\rm ms} \gtrsim$ 2–3 heat electrons beyond adiabatic compression via a two-step process: electrons accelerate in bulk along $\boldsymbol{B}$ towards the shock downstream, then relax into "flat-top" distributions in $\boldsymbol{B}$-parallel velocity (Feldman et al. 1982, 1983; Chen et al. 2018). Two mechanisms – quasi-static direct current (DC) fields and plasma waves – may drive $\boldsymbol{B}$-parallel acceleration. In the DC mechanism, an electric potential jump in the shock layer (i.e., a quasi-static electric field that points along shock normal) accelerates electrons in bulk (Feldman et al. 1983; Goodrich & Scudder 1984; Scudder et al. 1986; Scudder 1996; Hull et al. 2001; Lefebvre et al. 2007; Schwartz 2014). The DC electron energy gain scales with $\cos^2\theta$, where θ is the angle between $\boldsymbol{B}$ and shock normal (Goodrich & Scudder 1984). We expect no heating in exactly planar perpendicular shocks, but shock rippling from ion-scale waves (Lowe & Burgess 2003; Johlander et al. 2016; Hanson et al. 2019) can bend $\boldsymbol{B}$, alter θ, and enable DC heating. Plasma waves with non-zero $E_\parallel = \boldsymbol{E}\cdot\hat{\boldsymbol{b}}$, such as oblique whistlers, can also provide electron bulk acceleration and thus heating (Wilson et al. 2014a,b). Such plasma waves are intrinsic to shock structure (Wilson et al. 2009, 2012; Krasnoselskikh et al. 2002; Dimmock et al. 2019) and may be sustained by free energy from, e.g., shock-reflected ions (Wu et al. 1984; Matsukiyo & Scholer 2006; Muschietti & Lembège 2017).

In this Letter, we study thermal electron heating in multi-dimensional particle-in-cell (PIC) simulations of perpendicular shocks with realistic structure (requiring high ion/electron mass ratio $m_{\rm i}/m_{\rm e}$ (Krauss-Varban et al. 1995; Umeda et al. 2012a, 2014)) and high grid resolution to resolve electron scattering and relaxation after $\boldsymbol{B}$-parallel bulk acceleration.

2. METHOD

We simulate collisionless 2-D (x-y) ion-electron shocks using the relativistic particle-in-cell (PIC) code TRISTAN-MP (Buneman 1993; Spitkovsky 2005). We inject plasma with velocity $-u_0\hat{\boldsymbol{x}}$ and magnetic field $B_0\hat{\boldsymbol{y}}$ from the simulation domain's right-side (upstream) boundary. Injected plasma reflects from a conducting wall at $x = 0$, forming a shock that travels towards $+\hat{\boldsymbol{x}}$. The shocked downstream plasma has zero bulk velocity,

Corresponding author: Aaron Tran
aaron.tran@columbia.edu

and the upstream $\boldsymbol{B}$ is perpendicular to the shock normal, so $\theta = 90°$. The simulation domain expands along $+\hat{\boldsymbol{x}}$ to keep the right-side boundary $\gtrsim 1.5\ r_{\rm Li}$ ahead of the shock front (Sironi & Spitkovsky 2009, Sec. 2), where $r_{\rm Li} = u_0/\Omega_{\rm i}$ is a characteristic ion Larmor radius; we checked that shock heating physics is not artifically affected by the right-side boundary. Upstream ions and electrons have equal density n_0 and temperature T_0. The plasma frequencies $\omega_{\rm p\{i,e\}} = \sqrt{4\pi n_0 e^2/m_{\rm \{i,e\}}}$ and cyclotron frequencies $\Omega_{\rm \{i,e\}} = eB_0/(m_{\rm \{i,e\}}c)$ where subscripts i and e denote ions and electrons. We use Gaussian CGS units throughout.

Our fiducial simulations have ion/electron mass ratio $m_{\rm i}/m_{\rm e} = 625$ and total plasma beta $\beta_{\rm p} = 16\pi n_0 k_{\rm B} T_0/{B_0}^2 = 0.25$. The fast magnetosonic, sonic, and Alfvén Mach numbers are $\mathcal{M}_{\rm ms} = u_{\rm sh}/\sqrt{{c_{\rm s}}^2 + {v_{\rm A}}^2} = 1$–$10$, $\mathcal{M}_{\rm s} = u_{\rm sh}/c_{\rm s} = 3$–$20$, and $\mathcal{M}_{\rm A} = u_{\rm sh}/v_{\rm A} = 1.5$–$10$. The sound speed $c_{\rm s} = \sqrt{2\Gamma k_{\rm B} T_0/(m_i + m_e)}$, Alfvén speed $v_{\rm A} = B_0/\sqrt{4\pi n_0 (m_i + m_e)}$, and, $u_{\rm sh}$ is the speed of upstream plasma in the shock's rest frame; for non-relativistic speeds, $u_{\rm sh} = u_0/(1 - 1/r)$ where $r \leq 4$ is the MHD shock-compression ratio. The one-fluid adiabatic index Γ is not known a priori, but it is set self-consistently by the degree of ion and electron isotropization. We report Mach numbers assuming $\Gamma = 2$, which overestimates $\mathcal{M}_{\rm ms}$ by $\sim$1–10% for stronger shocks that isotropize ions/electrons and have $\Gamma \approx 5/3$.

The grid cell size $\Delta x = \Delta y = 0.1 c/\omega_{\rm pe}$ and the timestep $\Delta t = 0.045 {\omega_{\rm pe}}^{-1}$ so that $c = 0.45 \Delta x/\Delta t$. Upstream plasma has 16 particles per cell per species. We smooth the electric current with 32 sweeps of a three-point binomial ("1-2-1") filter at each timestep (Birdsall & Langdon 1991, Appendix C). The $N = 32$ sweeps approximate a Gaussian filter with standard deviation $\sqrt{N/2} = 4$ cells or $0.4 c/\omega_{\rm pe}$. The filter's half-power cut-off is at wavenumber $k \approx \sqrt{2/N}(\Delta x)^{-1} = 2.5\,(c/\omega_{\rm pe})^{-1}$, which implies 50% damping at wavelengths $\lambda \approx \pi\sqrt{2N}\Delta = 2.5\,(c/\omega_{\rm pe})$. Electron-scale waves may be damped, but we will later show that electron-scale waves mainly scatter rather than heat. We simulated 2-D $\mathcal{M}_{\rm ms} = 3.1$, $\beta_{\rm p} = 0.25$ shocks with $4\times$ larger or smaller sweep number N; the ratio $T_{\rm e}/T_{\rm i}$ did not change much. We adjust T_0, u_0, and B_0 to control $\mathcal{M}_{\rm ms}$ and $\beta_{\rm p}$ while keeping shocked electrons non-relativistic; i.e., post-shock $k_{\rm B} T_{\rm e} \lesssim 0.05 m_{\rm e} c^2$. The ratio $\tau = \omega_{\rm pe}/\Omega_{\rm e} = 2.5$–$11$ ($\tau \gg 1$ for solar wind and astrophysical settings). The transverse (y) width is 2.9–5.8 $c/\omega_{\rm pi} = 720$–1440 cells. Simulation durations are 10–20 ${\Omega_{\rm i}}^{-1} = 932$–$2736\ {\omega_{\rm pi}}^{-1}$ so that post-shock $T_{\rm e}/T_{\rm i}$ reaches steady state. The temperatures $T_{\rm \{i,e\}}$, $T_{\rm \{i,e\}\parallel}$, and $T_{\rm \{i,e\}\perp}$ are moments of the particle distribution in a 5^N cell region, where $N \in \{1, 2, 3\}$ is the domain dimensionality. The co-moving frame boost for moment calculation uses a fluid velocity also averaged over 5^N cells. All $\parallel$- and $\perp$-subscripted quantities are taken with respect to local $\boldsymbol{B}$.

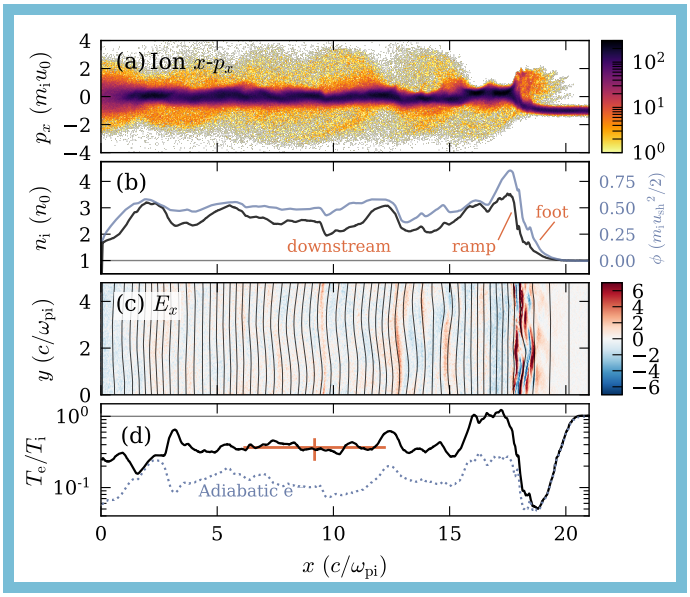


Figure 1. Overview of $\mathcal{M}_{\rm ms} = 3.1$, $\beta_{\rm p} = 0.25$ shock at $t = 1253\ {\omega_{\rm pi}}^{-1} = 14.2\ {\Omega_{\rm i}}^{-1}$. (a) Ion x-p_x phase-space distribution for full domain, where p_x is ion x-momentum normalized to upstream momentum $m_{\rm i}u_0$. (b) Ion density $n_{\rm i}/n_0$ (black) and electromotive force $\phi(x) = -\int_\infty^x E_x(x')\mathrm{d}x'$ in units of $m_{\rm i}{u_{\rm sh}}^2/2$ (light blue). Both curves are 1-D volume-weighted averages over y. The shock foot, ramp, and downstream are annotated. (c) Electric field E_x normalized to upstream motional field $u_0 B_0/c$ with magnetic field lines overlaid. $\boldsymbol{B}$ points up; i.e., along $+\hat{\boldsymbol{y}}$. (d) $T_{\rm e}/T_{\rm i}$, density-weighted y average (black), compared to prediction for fluid adiabatic electron heating defined in text (blue dotted). Orange cross is starred measurement in Fig. 2(a); cross width is measurement region, and cross height is standard deviation over 2-D region delimited by cross width. An animation of this figure in the online journal plots shows time evolution from $t = 0$ to $1253\ {\omega_{\rm pi}}^{-1}$ and demonstrates that the temperature ratio $T_{\rm e}/T_{\rm i}$ stabilizes $\sim 3\ c/\omega_{\rm pi}$ downstream of the shock ramp.

Fig. 1 shows a representative simulation. Ions transmit or reflect at the shock ramp (Fig. 1(a-b)). The shock front is rippled (Fig. 1(c)). A net E_x potential exists across the shock, and E_x is also modulated by the $\boldsymbol{B}$ rippling wavelength (Fig. 1(b-c)). Reflected ions accelerate in the motional field $E_z = u_0 B_0/c$ before re-entering the shock (Leroy et al. 1982); this lowers $T_{\rm e}/T_{\rm i}$ in the shock foot (Fig. 1(d)). Electrons heat above adiabatic expectation in the shock ramp and settle to $T_{\rm e}/T_{\rm i} \approx 0.4$; no appreciable heating occurs after the shock ramp (Fig. 1(d)). The fluid adiabatic prediction in Fig. 1(d) is $T_{\rm e,ad}/(T_{\rm i} + T_{\rm e} - T_{\rm e,ad})$, using measured $T_{\rm i}$ and $T_{\rm e}$ and assuming $T_{\rm e,ad} = T_0[1 + 2(n/n_0)^{\Gamma-1}]/3$ with $\Gamma = 2$.

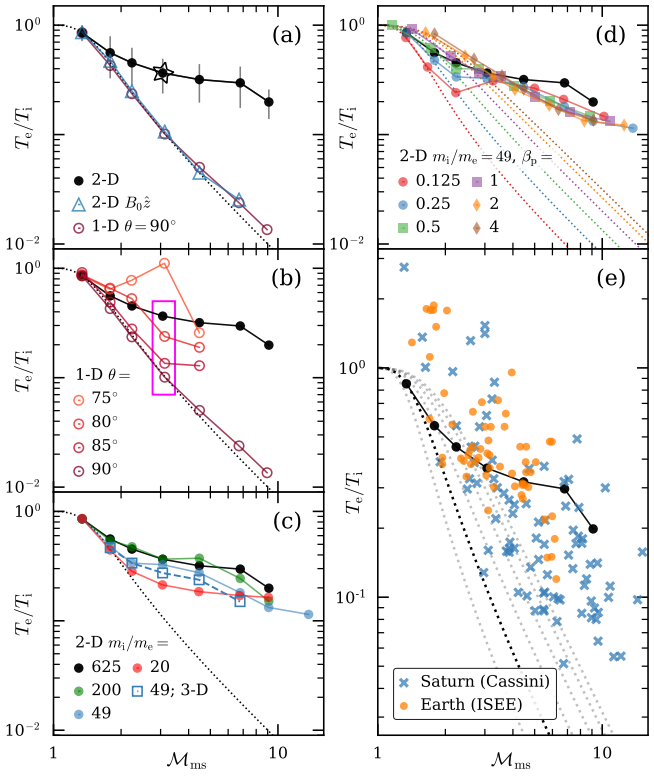


Figure 2. Post-shock T_e/T_i dependence on $\mathcal{M}_{ms}$ for various setups. All panels: black curve is T_e/T_i from fiducial 2-D $m_i/m_e = 625$, $\beta_p = 0.25$ shocks. Dotted curves are expected T_e/T_i from MHD shock jump conditions, assuming adiabatic electron heating alone. (a): Varying geometry. 2-D domain with out-of-plane $B_0\hat{\boldsymbol{z}}$ (triangles) and 1-D domain (hollow circles). Starred datum appears in Figs. 1, 3–4. Error bars on black curve are standard deviation of T_e/T_i within measurement region. (b): 1-D domain, varying θ. Darkest hollow circles ($\theta = 90°$) same as (a). (c): 2-D domain, varying m_i/m_e. Dashed cyan curve with square markers comprises 3-D $m_i/m_e = 49$ simulations. (d): 2-D domain, $m_i/m_e = 49$, varying β_p. Dotted curves are adiabatic expectation as in panels (a-c), with β_p increasing from left to right. (e): Comparison to solar wind bow shock measurements at Earth (orange circles) (Schwartz et al. 1988) and Saturn (blue crosses) (Masters et al. 2011) as compiled by (Ghavamian et al. 2013). Five Saturn measurements with $\mathcal{M}_{ms} > 20$ are not shown.

3. SHOCK PARAMETER SCALING

We measure post-shock T_e/T_i (Fig. 1(c)) as a function of $\mathcal{M}_{ms}$ for many simulations with varying dimensionality, magnetic field orientation θ, m_i/m_e, and β_p. We also adjust domain width, particle resolution, and current smoothing to control noise and computing cost. In simulations with $\theta < 90°$, the right-side boundary expands at $\max(u_{sh}, 0.5c\cos\theta)$ to retain shock-reflected electrons streaming along $\boldsymbol{B}$.

We show the post-shock T_e/T_i for our fiducial 2-D $m_i/m_e = 625$ shocks with in-plane upstream magnetic field $B_0\hat{\boldsymbol{y}}$ in Fig. 2(a). These fiducial simulations are converged in T_e/T_i with respect to transverse (y) width. For perpendicular shocks, we find that electron heating beyond adiabatic compression requires 2-D geometry with in-plane $\boldsymbol{B}$. Corresponding 2-D simulations with out-of-plane $\boldsymbol{B}$ (along $\hat{\boldsymbol{z}}$) and 1-D simulations heat electrons by compression alone (Fig. 2(a)). At $\mathcal{M}_{ms} \sim 5$–10, the 2-D simulations with out-of-plane $\boldsymbol{B}$ and 1-D simulations show weak super-adiabatic heating in the shock layer, but the T_e/T_i measurement is also less precise due to numerical heating. Shimada & Hoshino (2000, 2005) saw strong electron heating in 1-D perpendicular $m_i/m_e = 20$ shocks due to Buneman instability between shock-reflected ions and incoming electrons. The higher $m_i/m_e = 625$ suppresses the Buneman instability in our 1-D shocks.

Can DC heating in a 2-D rippled shock – i.e., varying local magnetic field angle due to self-generated waves – explain the super-adiabatic electron heating seen in our fiducial 2-D simulations? To estimate the DC heating from varying θ, we perform 1-D oblique shock simulations with varying $\theta < 90°$ (Fig. 2(b)); recall that θ is the angle between $\boldsymbol{B}$ and shock normal. The 1-D setup keeps quasi-static shock structure (averaged over shock reformation cycles) and should retain DC heating while excluding waves oblique to the shock normal. We do find super-adiabatic heating in 1-D oblique shocks. Electrons heat more for lower θ, which is qualitatively consistent with DC field heating (Goodrich & Scudder 1984). For our representative $\mathcal{M}_{ms} = 3.1$ shock, which has local ripple $\theta \gtrsim 80°$ (Fig. 4(f)), the DC heating inferred from 1-D oblique shock simulations appears too low to explain the full amount of super-adiabatic heating (Fig. 2(b, box)).

Our fiducial 2-D perpendicular shocks appear converged in mass ratio at $m_i/m_e \sim 200$–625 (Fig. 2(c)), consistent with prior simulations (Umeda et al. 2012a, 2014) and theory (Krauss-Varban et al. 1995). For $m_i/m_e = 20$–625, 2-D shocks agree on T_e/T_i to within a factor of 2–3. A set of 3-D $m_i/m_e = 49$ simulations with narrower transverse width, $2.7c/\omega_{pi}$, shows good agreement too. Agreement between 2-D and 3-D for $m_i/m_e = 49$ suggests that 2-D simulations with in-plane $\boldsymbol{B}$ include the essential physics for electron heating.

To see how heating depends on β_p, we reduce m_i/m_e to 49 and sweep β_p over 0.125–4 (Fig. 2(d)). Electron heating increases above adiabatic at $\mathcal{M}_{ms} \sim 2$–3 for all β_p. At $\mathcal{M}_{ms} \sim 3$–5 and $\beta_p \leq 1$, two-step $\boldsymbol{B}$-parallel electron heating (which we describe below) operates for all $\beta_p \lesssim 1$. At $\mathcal{M}_{ms} \sim 3$–5 and $\beta_p \gtrsim 2$, a distinct electron cyclotron whistler instability is expected to heat electrons instead (Guo et al. 2017, 2018). At $\mathcal{M}_{ms} \gtrsim 5$, shock structure is more complex, which we do not explore here. The relationship between T_e/T_i and $\mathcal{M}_{ms}$ does not appear to depend on β_p for $\mathcal{M}_{ms} \gtrsim 4$.

Our fiducial T_e/T_i–$\mathcal{M}_{ms}$ data are order-of-magnitude consistent with measurements from solar wind bow

shocks (Fig. 2(e)), replotted from Ghavamian et al. (2013). The Saturn data are uncertain in both T_e/T_i and $\mathcal{M}_{ms}$ due to a lack of ion temperature measurements from Cassini (Masters et al. 2011), so $\mathcal{M}_{ms} = 0.671\mathcal{M}_A$ (equivalent to $\beta_p \sim 1.5$) is assumed following Ghavamian et al. (2013); we note $\beta_p \sim 1.5$ is a typical value (Richardson 2002). The Earth data have $\beta_p \sim 0.1$–1 and use directly measured ion and electron temperatures from the ISEE spacecraft (Schwartz et al. 1988). Both datasets are mostly quasi-perpendicular, with a majority of shocks having $50° < \theta < 90°$ (Schwartz et al. 1988; Masters et al. 2011).

4. ELECTRON HEATING PHYSICS

For further study, we choose the weakest 2-D $m_i/m_e = 625$, $\beta_p = 0.25$ shock with significant super-adiabatic heating: our representative $\mathcal{M}_{ms} = 3.1$ simulation (Fig. 1, 2(a)). We redo this simulation with higher resolution: $\Delta x = \Delta y = 0.05\ c/\omega_{pe}$ (keeping $c = 0.45\Delta x/\Delta t$), 64 particles per cell per species, and 64 current filter passes per timestep. The current filter approximates a Gaussian with standard deviation ∼5.7 cells or $0.28c/\omega_{pe}$; the filter's half-power cut-off is at wavenumber $k \approx 3.5\,(c/\omega_{pe})^{-1}$, which means 50% damping at wavelength $\lambda \approx 1.8c/\omega_{pe}$. We then select all 15898 electron particles between $x = 8.00$–$8.02\ c/\omega_{pi}$ at $t' \equiv t - 324\ \omega_{pi}{}^{-1} = 0$, located $4\ c/\omega_{pi} = 2\ r_{Li}$ ahead of the shock ramp, and monitor their phase space evolution (Fig. 3) and energy gain (Fig. 4) through the shock. The perpendicular upstream $\boldsymbol{B}$ confines particles within a narrow magnetic flux tube and prevents particle drift from downstream to upstream.

Elongated, ion-scale $E_\parallel$ waves accelerate electrons along $\boldsymbol{B}$ in the shock foot and ramp. These waves have $|E_\parallel|/(u_0B_0/c) \sim 0.2$–$0.6$ and wavelength $\lambda_y \sim 2c/\omega_{pi} \sim r_{Li}$ (Fig. 3(a), arrow); we attribute this $E_\parallel$ to very oblique whistler waves (i.e., magnetosonic / lower hybrid branch) with fluctuating $E_x \gg E_y, E_z$ and $B_y, B_z > B_x$, as identified by prior PIC studies (Matsukiyo & Scholer 2003; Hellinger et al. 2007; Matsukiyo & Scholer 2006; Umeda et al. 2012b). A stronger bipolar ion-scale $|E_\parallel|/(u_0B_0/c) \gtrsim 0.5$ (Fig. 3(b), arrow) straddles clumps of shock-reflected ions and also accelerates electrons. Accelerated electrons appear as coherent deflections in $\gamma\beta_\parallel$–y phase space (Fig. 3(g-h), arrows) that disrupt and relax via two-stream-like instability. Local y-regions develop asymmetric and transiently unstable $\gamma\beta_\parallel$ distributions (Fig. 3(q,v,x)). Electron relaxation generates strong and rapid electron-scale $E_\parallel$ waves and phase-space holes with $\lambda_y \sim c/\omega_{pe}$ (Fig. 3(b,g,i), boxes) (cf. An et al. 2019) Landau damping is evidenced by flattened distributions at $\gamma\beta_\parallel \sim 0.2$ (Fig. 3(k-l)). Electrons relax to near isotropy by $t' \sim 140\ \omega_{pi}{}^{-1}$ (Fig. 3(j,o,t,y)). Prior 2-D PIC simulations have shown similar two-step $\boldsymbol{B}$-parallel heating in a shock foot setup (periodic inter-

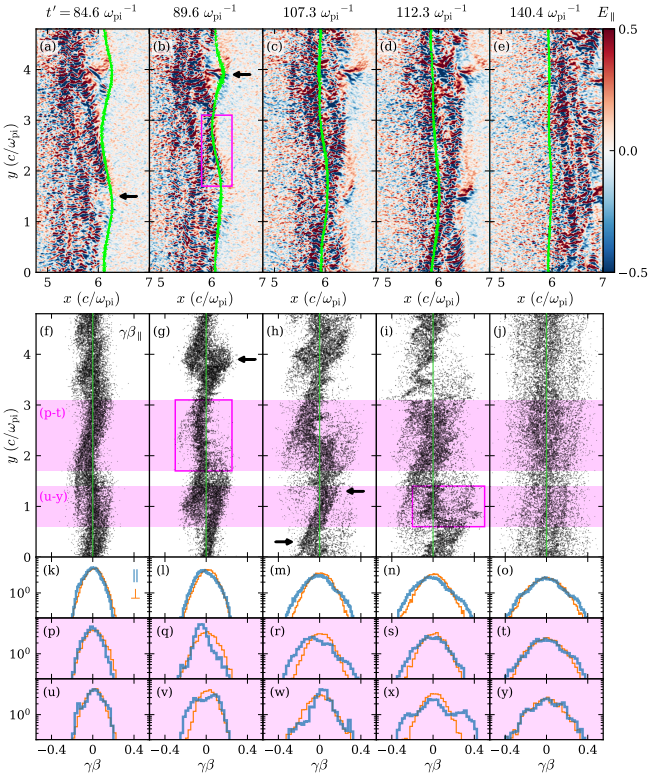


Figure 3. Phase space time evolution (left to right) of electron sample in $\mathcal{M}_{ms} = 3.1$, $\beta_p = 0.25$ shock. (a-e): $E_\parallel$ normalized to upstream motional field u_0B_0/c with electron sample overlaid (green dots). Colormap saturates on small-scale waves. (f-j): $\gamma\beta_\parallel$–y phase space of electron sample. Green vertical lines mark $\gamma\beta_\parallel = 0$. (k-o): 1-D $\gamma\beta_{\{\parallel,\perp\}}$ distribution of full electron sample. Thick blue curve is $\gamma\beta_\parallel$; orange curve is $\gamma\beta_\perp$. (p-t): like (k-o), but only electrons within $y = 1.7$–$3.1\ c/\omega_{pi}$. (u-y): like (k-o), but only electrons within $y = 0.6$–$1.4\ c/\omega_{pi}$. Here $\gamma = 1/\sqrt{1-\beta^2}$ and $\beta_{\{\parallel,\perp\}} = v_{\{\parallel,\perp\}}/c$. Arrows and boxes discussed in text.

penetrating beams) (Matsukiyo & Scholer 2006) and in full shocks (Umeda et al. 2011, 2012b).

$E_\parallel$ is the main source of non-adiabatic electron heating (Fig. 4(a)). We decompose the sample electrons' mean energy gain W_{tot} into parallel and perpendicular work, $W_\parallel = -e\langle\int E_\parallel v_\parallel dt\rangle$ and $W_\perp = -e\langle\int E_\perp v_\perp dt\rangle$, integrated for every particle over every code timestep Δt such that $W_{tot} = W_\parallel + W_\perp$. Angle brackets are particle averages. We estimate the adiabatic heating as $W_{\perp,ad} = \langle\sum_n(\gamma_{n\to n+1,ad} - \gamma_n)m_ec^2\rangle$, where

$$\gamma_{n\to n+1,ad} = \sqrt{1 + (\gamma\beta_\parallel)_n^2 + (\gamma\beta_\perp)_n^2\,(B_{n+1}/B_n)} \quad (1)$$

captures electron heating from compression between timesteps n and $n+1$.

In Eqn. (1), we assume $(\gamma\beta_\perp)_n^2/B_n$ and $(\gamma\beta_\parallel)_n$ are constant during compression; γ, $\beta_\parallel$, and $\beta_\perp$ are evaluated in the electron fluid's rest frame. The sum in

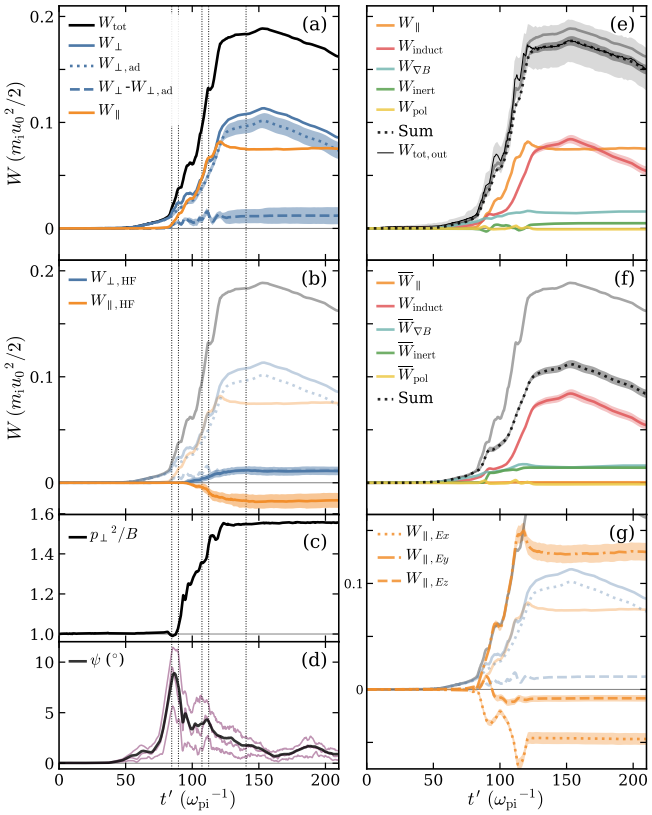


Figure 4. Mean work done on electron sample over time, normalized to upstream ion drift kinetic energy. Vertical dotted lines are snapshot times in Fig. 3. Faded curves in (b,e,f,g) same as (a). Shaded regions are estimated error on coarse-timestep integrated quantities. (a): Decomposition into $W_\parallel$, $W_\perp$ and adiabatic work $W_{\perp,\rm ad}$. (b): High-frequency electric field work. (c): Particle-averaged adiabatic moment $p_\perp{}^2/B$, scaled to mean upstream value. (d): Magnetic field tilt $\psi = \tan^{-1}\left(B_x/\sqrt{B_y{}^2 + B_z{}^2}\right)$ with respect to y-z plane. Black curve is particle average $\langle\psi\rangle$; purple curves are 25th, 50th (median), and 75th percentiles. (e): Parallel, induction, ∇B, inertial, and polarization work. Dark-gray region is error for sum of drift work; light-gray region is error for $W_{\rm tot,out}$. (f): DC-like drift work, defined in text. (g): Parallel work contributions from E_x, E_y, and E_z, as defined in text. The y-axis is offset from (a-b,e-f).

$W_{\perp,\rm ad}$ uses a coarse output timestep $\Delta t_{\rm out} = 400\ \Delta t = 9\ \omega_{\rm pe}{}^{-1}$.

The non-adiabatic perpendicular work can be explained by high-frequency scattering of electron parallel energy into perpendicular energy (Fig. 4(b)). We Fourier-space filter E_x, E_y, and E_z to isolate wavenumbers $k_y > (c/\omega_{\rm pe})^{-1}$ and then construct $E_{\perp,\rm HF}$ and $E_{\parallel,\rm HF}$ by projecting the Fourier-filtered fields onto local $\boldsymbol{B}$. Then, $W_{\perp,\rm HF} = -e\langle\sum E_{\perp,\rm HF} v_\perp \Delta t_{\rm out}\rangle$ and $W_{\parallel,\rm HF} = -e\langle\sum E_{\parallel,\rm HF} v_\parallel \Delta t_{\rm out}\rangle$. We find that $W_{\perp,\rm HF}$ and $W_\perp - W_{\perp,\rm ad}$ agree to $\sim 10\%$, suggesting that non-adiabatic $W_\perp$ comes from electron-scale scattering of parallel energy. Exact agreement is not expected due to the coarse timestep $\Delta t_{\rm out}$ and the arbitrary k_y cut.

The particle-averaged adiabatic moment $p_\perp{}^2/B$ grows in steps that correlate with increases in $W_{\rm tot}$ and $W_\parallel$. Bulk acceleration at $t' = 84.6\ \omega_{\rm pi}{}^{-1}$ and $t' = 107.3\ \omega_{\rm pi}{}^{-1}$ coincides with momentarily constant $p_\perp{}^2/B$ and increasing $W_\parallel$ prior to a scattering episode. Then, $p_\perp{}^2/B$ increases during strong electron scattering at $t' = 89.6\ \omega_{\rm pi}{}^{-1}$ and $112.3\ \omega_{\rm pi}{}^{-1}$ while $W_\parallel$ flattens off (Fig. 3, Fig. 4(a,c)).

Fig. 4(e) shows mean work from grad B, inertial, and polarization drifts, as well as $\partial B/\partial t$ induction work; see Northrop (1961, 1963); Goodrich & Scudder (1984); Dahlin et al. (2014); Rowan et al. (2019). Each $W_{\rm drift} = -e\langle\sum \boldsymbol{E}\cdot\boldsymbol{v}_{\rm drift}\Delta t_{\rm out}\rangle$, where $\boldsymbol{v}_{\rm drift}$ is one of:

$$\boldsymbol{v}_{\{\nabla B,\rm inert,pol\}} = -\frac{\gamma m_e c}{eB}\hat{\boldsymbol{b}}\times\left\{\frac{v_\perp{}^2}{2B}\nabla B,\ v_\parallel\frac{\mathrm{d}\hat{\boldsymbol{b}}}{\mathrm{d}t},\ \frac{\mathrm{d}\boldsymbol{v}_E}{\mathrm{d}t}\right\},$$

with γ and $v_\perp$ evaluated in the electron fluid's rest frame. We take $\boldsymbol{v}_E = \langle c\boldsymbol{E}\times\boldsymbol{B}/B^2\rangle$ to reduce noise; otherwise, the $\boldsymbol{v}_{\rm drift}$ terms use $\boldsymbol{E}$ and $\boldsymbol{B}$ fields seen by individual particles. The $\mathrm{d}/\mathrm{d}t$ terms are one-sided finite differences; e.g., $\mathrm{d}\boldsymbol{v}_E/\mathrm{d}t = [(\boldsymbol{v}_E)_{n+1} - (\boldsymbol{v}_E)_n]/\Delta t_{\rm out}$. And, $W_{\rm induct} = \gamma m_e v_\perp{}^2(\partial B/\partial t)/(2B)$, with $\partial B/\partial t = [B_{n+1}(\boldsymbol{r}_n) - B_{n-1}(\boldsymbol{r}_n)]/(2\Delta t_{\rm out})$ and $\boldsymbol{r}_n$ the particle position at timestep n. We find that grad B drift and induction together give fluid-like adiabatic compression. Inertial and polarization drifts give less work, but some other electron samples have $W_{\rm inert}$ comparable to $W_{\nabla B}$ (Appendix A). We compare the summed drifts to $W_{\rm tot,out} = -e\langle\sum \boldsymbol{E}\cdot\boldsymbol{v}\Delta t_{\rm out}\rangle$. We conclude that $W_{\rm tot}$ agrees with both the summed drift work and $W_{\rm tot,out}$, given uncertainty from both the guiding-center drift approximation and the coarse integration timestep.

Earlier, we argued that DC heating alone may not explain all super-adiabatic heating in our fiducial 2-D shock, based on downstream volume-averaged T_e/T_i (Figs. 1(c), 2(b)). So, Fig. 4(f) estimates DC-like work as $\overline{W}_{\rm drift} = -e\sum\langle\boldsymbol{E}\rangle\cdot\langle\boldsymbol{v}_{\rm drift}\rangle\Delta t_{\rm out}$ and $\overline{W}_\parallel = -e\sum\langle E_\parallel\rangle\langle v_\parallel\rangle\Delta t_{\rm out}$. The $\boldsymbol{E}$ average removes waves along $\hat{\boldsymbol{y}}$ to keep only 1-D-like shock fields. The $\boldsymbol{v}_{\rm drift}$ average gives a mean drift trajectory and mostly discards gyration. The DC-like parallel work $\overline{W}_\parallel$ goes to zero, and the DC-like contribution to super-adiabatic heating appears small. Fluid-like adiabatic compression is preserved in $W_{\rm induct} + \overline{W}_{\nabla B}$. Fig. 4(g) separates E_x, E_y, and E_z contributions to $W_\parallel$ as $W_{\parallel,Ei} = -e\langle\sum E_i b_i v_\parallel\Delta t_{\rm out}\rangle$, where $i = x, y, z$ and b_i is the i-th component of $\hat{\boldsymbol{b}}$. E_y gives parallel heating, whereas E_x and E_z cause parallel cooling.

The quantities $W_{\perp,\rm ad}$, $W_{\{\parallel,\perp\},\rm HF}$, $W_{\rm drift}$, $W_{\rm tot,out}$, $\overline{W}_{\rm drift}$, $\overline{W}_\parallel$, and $W_{\parallel,Ei}$ are integrated with coarse timestep $\Delta t_{\rm out}$ and converged at the $\sim$10% level. The error regions in Fig. 4(a,b,e) are defined in Appendix B.

5. CONCLUSION

We have measured T_e/T_i in 2-D PIC simulations of perpendicular shocks to inform models of astrophysical systems lacking direct T_e or T_i measurements. In a $\mathcal{M}_{ms} = 3.1$, $\beta_p = 0.25$ rippled shock, quasi-static DC fields provide fluid-like adiabatic heating, and most super-adiabatic heating is from ion-scale $E_\parallel$ waves.

ACKNOWLEDGMENTS

Xinyi Guo shared and provided helpful assistance for some software used to perform and analyze these simulations. Alex Bergier and colleagues provided excellent assistance with Columbia's Habanero cluster. Adam Masters and Parviz Ghavamian kindly shared Saturn bow shock data. We thank Matthew W. Abruzzo, Luca Comisso, Greg Howes, Anatoly Spitkovsky, Vassilis Tsiolis, and Lynn B. Wilson III for discussion. We thank the anonymous referees for integral comments and critiques. LS and AT were supported by the Sloan Fellowship to LS, NASA ATP-80NSSC20K0565, and NSF AST-1716567. Some work was done at UCSB KITP, which is supported by NSF PHY-1748958. Simulations were run on Habanero (Columbia University), Edison (NERSC), and Pleiades (NASA HEC). Columbia University's Shared Research Computing Facility is supported by NIH Research Facility Improvement Grant 1G20RR030893-01 and the New York State Empire State Development, Division of Science Technology and Innovation (NYSTAR) Contract C090171. NERSC is a U.S. Department of Energy Office of Science User Facility operated under Contract DE-AC02-05CH11231. The NASA HEC Program is part of the NASA Advanced Supercomputing (NAS) Division at Ames Research Center.

Facility: NERSC, Pleiades

REFERENCES

An, X., Li, J., Bortnik, J., et al. 2019, PhRvL, 122, 045101

Avestruz, C., Nagai, D., Lau, E. T., & Nelson, K. 2015, ApJ, 808, 176

Birdsall, C. K., & Langdon, A. B. 1991, Plasma Physics via Computer Simulation, The Adam Hilger Series on Plasma Physics (Bristol, England: IOP Publishing Ltd)

Buneman, O. 1993, in Computer Space Plasma Physics: Simulation Techniques and Software, ed. H. Matsumoto & Y. Omura (Tokyo: Terra Scientific), 67–84

Chen, L.-J., Wang, S., Wilson, III, L. B., et al. 2018, Physical Review Letters, 120, 225101

Cohen, I. J., Schwartz, S. J., Goodrich, K. A., et al. 2019, Journal of Geophysical Research (Space Physics), 124, 3961

Dahlin, J. T., Drake, J. F., & Swisdak, M. 2014, Physics of Plasmas, 21, 092304

Dimmock, A. P., Russell, C. T., Sagdeev, R. Z., et al. 2019, Science Advances, 5, eaau9926

Feldman, W. C., Bame, S. J., Gary, S. P., et al. 1982, Physical Review Letters, 49, 199

Feldman, W. C., Anderson, R. C., Bame, S. J., et al. 1983, J. Geophys. Res., 88, 96

Ghavamian, P., Schwartz, S. J., Mitchell, J., Masters, A., & Laming, J. M. 2013, SSRv, 178, 633

Goodrich, C. C., & Scudder, J. D. 1984, J. Geophys. Res., 89, 6654

Goodrich, K. A., Ergun, R., Schwartz, S. J., et al. 2018, Journal of Geophysical Research (Space Physics), 123, 9430

Guo, X., Sironi, L., & Narayan, R. 2014, ApJ, 794, 153

—. 2017, ApJ, 851, 134

—. 2018, ApJ, 858, 95

Hanson, E. L. M., Agapitov, O. V., Mozer, F. S., et al. 2019, Geophys. Res. Lett., 46, 2381

Helder, E. A., Kosenko, D., & Vink, J. 2010, ApJL, 719, L140

Hellinger, P., Trávníček, P., Lembège, B., & Savoini, P. 2007, Geophys. Res. Lett., 34, L14109

Hovey, L., Hughes, J. P., McCully, C., Pandya, V., & Eriksen, K. 2018, ApJ, 862, 148

Hull, A. J., Scudder, J. D., Larson, D. E., & Lin, R. 2001, J. Geophys. Res., 106, 15711

Johlander, A., Schwartz, S. J., Vaivads, A., et al. 2016, PhRvL, 117, 165101

Krasnoselskikh, V. V., Lembège, B., Savoini, P., & Lobzin, V. V. 2002, Physics of Plasmas, 9, 1192

Krauss-Varban, D., Pantellini, F. G. E., & Burgess, D. 1995, Geophys. Res. Lett., 22, 2091

Lefebvre, B., Schwartz, S. J., Fazakerley, A. F., & Décréau, P. 2007, Journal of Geophysical Research (Space Physics), 112, A09212

Leroy, M. M., Winske, D., Goodrich, C. C., Wu, C. S., & Papadopoulos, K. 1982, J. Geophys. Res., 87, 5081

Lowe, R. E., & Burgess, D. 2003, Annales Geophysicae, 21, 671

Masters, A., Schwartz, S. J., Henley, E. M., et al. 2011, Journal of Geophysical Research (Space Physics), 116, A10107

Matsukiyo, S., & Scholer, M. 2003, Journal of Geophysical Research (Space Physics), 108, 1459

—. 2006, Journal of Geophysical Research (Space Physics), 111, A06104

Muschietti, L., & Lembège, B. 2017, Annales Geophysicae, 35, 1093

Northrop, T. G. 1961, Annals of Physics, 15, 79

—. 1963, Reviews of Geophysics and Space Physics, 1, 283

Richardson, J. D. 2002, Planet. Space Sci., 50, 503

Rowan, M. E., Sironi, L., & Narayan, R. 2019, ApJ, 873, 2

Schwartz, S. J. 2014, Journal of Geophysical Research (Space Physics), 119, 1507

Schwartz, S. J., Thomsen, M. F., Bame, S. J., & Stansberry, J. 1988, J. Geophys. Res., 93, 12923

Scudder, J. D. 1996, J. Geophys. Res., 101, 2561

Scudder, J. D., Mangeney, A., Lacombe, C., et al. 1986, J. Geophys. Res., 91, 11075

Shimada, N., & Hoshino, M. 2000, ApJL, 543, L67

—. 2005, Journal of Geophysical Research (Space Physics), 110, A02105

Sironi, L., & Spitkovsky, A. 2009, ApJ, 698, 1523

Spitkovsky, A. 2005, in AIP Conference Proceedings, Vol. 801, Astrophysical Sources of High Energy Particles and Radiation, ed. T. Bulik, B. Rudak, & G. Madejski (Melville, New York: American Institute of Physics), 345–350

Umeda, T., Kidani, Y., Matsukiyo, S., & Yamazaki, R. 2012a, Physics of Plasmas, 19, 042109

—. 2012b, Journal of Geophysical Research (Space Physics), 117, A03206

—. 2014, Physics of Plasmas, 21, 022102

Umeda, T., Yamao, M., & Yamazaki, R. 2011, Planet. Space Sci., 59, 449

Wilson, L. B., I., Cattell, C. A., Kellogg, P. J., et al. 2009, Journal of Geophysical Research (Space Physics), 114, A10106

Wilson, L. B., Sibeck, D. G., Breneman, A. W., et al. 2014a, Journal of Geophysical Research (Space Physics), 119, 6455

—. 2014b, Journal of Geophysical Research (Space Physics), 119, 6475

Wilson, III, L. B., Koval, A., Szabo, A., et al. 2012, Geophys. Res. Lett., 39, L08109

Wu, C. S., Winske, D., Zhou, Y. M., et al. 1984, SSRv, 37, 63

Yamaguchi, H., Eriksen, K. A., Badenes, C., et al. 2014, ApJ, 780, 136

APPENDIX

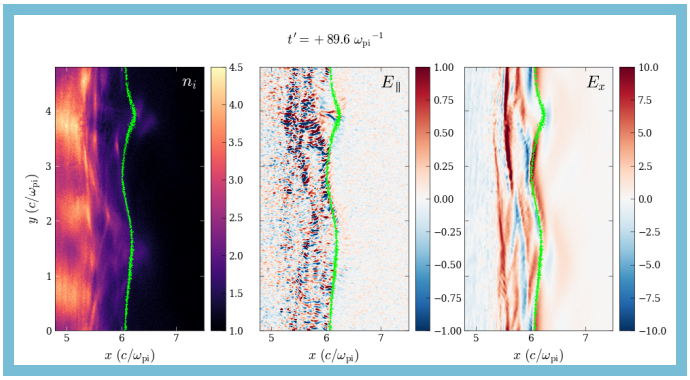


Figure 5. Movie still: electron sample at $t' = 89.6\ \omega_{\rm pi}{}^{-1}$ plotted over ion density $n_{\rm i}$, parallel electric field $E_\parallel$, and electric field component E_x; same sample from Figs. 3 and 4. An animation of this figure from $t' = 54$ to $180\ \omega_{\rm pi}{}^{-1}$. is in the online journal. The ion density $n_{\rm i}$ is scaled to upstream density n_0, and the electric field components are scaled to upstream motional electric field magnitude $u_0 B_0/c$. The $E_\parallel$ colormap spans $[-1, +1]$ and saturates on small-scale waves, despite being a wider range than Fig. 3.

A. MORE VIEWS OF ELECTRON SAMPLE HEATING

Figs. 5 and 6 present two movies, available online, of our electron sample traversing the shock front.

In Fig. 7, we show the work decomposition from Fig. 4 for many electron samples. At $t' = 0\ \omega_{\rm pi}{}^{-1}$, we selected all electrons in the regions $x \in [5.60, 5.62] c/\omega_{\rm pi}$, $x \in [6.00, 6.02] c/\omega_{\rm pi}$, and so on with even spacing $0.4 c/\omega_{\rm pi}$ to get seventeen electron particle samples of similar size.

Fig. Set 7. Electron Work Decomposition

B. CONVERGENCE IN ELECTRON WORK SUMMATION

Several quantities in Figure 4 are summed with a coarse timestep $\Delta t_{\rm out} = 400 \Delta t = 9\ \omega_{\rm pe}{}^{-1}$, namely: $W_{\perp,\rm ad}$, $W_\perp - W_{\perp,\rm ad}$, $W_{\perp,\rm HF}$, $W_{\parallel,\rm HF}$, $W_{\rm induct}$, $W_{\nabla \rm B}$, $W_{\rm inert}$, $W_{\rm pol}$, $W_{\rm tot,out}$, $\overline{W}_{\nabla \rm B}$, $\overline{W}_{\rm inert}$, $\overline{W}_{\rm pol}$, $\overline{W}_\parallel$, $W_{\parallel,Ex}$, $W_{\parallel,Ey}$, and $W_{\parallel,Ez}$. To check convergence, we downsample in time each quantity's summand by 4 and compute an error δf at discrete time t_n as:

$$\delta f(t_n) = \max\left\{ \left| f(t_m) - f_{1/4}(t_m) \right| \mid 0 \le m \le n \right\} \quad \text{(B1)}$$

where $f_{1/4}$ is the $4\times$ downsampled version of f. Thus δf is strictly non-decreasing with t_n. The error regions defined by Eq. B1 are plotted as shaded areas in Figs. 4 and 7.

Fig. 8 shows curves with $2, 4, 8\times$ downsampling for the seventeen distinct electron samples of Fig. 7, including the sample shown in Fig. 4.

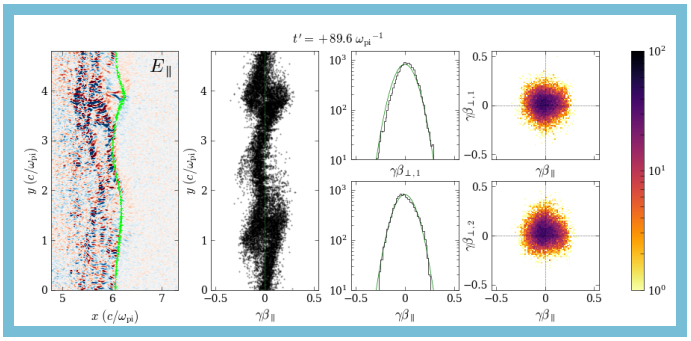


Figure 6. Movie still: electron sample phase space at $t' = 89.6\ \omega_{\rm pi}{}^{-1}$, with more detail than Fig. 3. An animation of this figure from $t' = 54$ to $180\ \omega_{\rm pi}{}^{-1}$. is in the online journal. The momentum component $\gamma\beta_{\perp,1}$ is the projection along $(\hat{\boldsymbol{b}} \times -\hat{\boldsymbol{x}}) \times \hat{\boldsymbol{b}}$, and the component $\gamma\beta_{\perp,2}$ is the projection along $\hat{\boldsymbol{b}} \times -\hat{\boldsymbol{x}}$. Because the local magnetic field unit vector $\hat{\boldsymbol{b}}$ mostly orients along $\hat{\boldsymbol{y}}$, the components $\perp, 1$ and $\perp, 2$ roughly correspond to $-\hat{\boldsymbol{x}}$ and $+\hat{\boldsymbol{z}}$ so that $(\perp, 1;\ \perp, 2;\ \parallel)$ form a right-handed coordinate system. In the 1-D phase space plots, the light green curve is an isotropic Maxwell-Jüttner distribution with same mean energy as the electrons. The $E_\parallel$ colormap is the same as in Fig. 5.

Fig. Set 8. Electron Work Convergence

C. TRANSVERSE WIDTH CONVERGENCE

Fig. 9 shows that our fiducial 2-D simulations are converged with respect to transverse width. Most of the varying transverse width simulations are *not* listed in Table 1. For $\mathcal{M}_{\rm ms} = 9.1$ only, the 1-D simulation uses a slightly higher upstream temperature than the 2-D simulations, so the ratio $\Omega_{\rm i}/\omega_{\rm pi}$ differs between 1-D and 2-D. In this case, we matched times based on $\Omega_{\rm i}{}^{-1}$ rather than $\omega_{\rm pi}{}^{-1}$.

D. SIMULATION PARAMETERS

Table 1 contains input parameters, derived shock parameters, run durations, and downstream temperature measurements for all simulations in our manuscript. The first row is the high-resolution run used in Figs. 3 and 4; the remaining rows are presented in Fig. 2. A machine-readable version of Table 1, in comma-separated value (CSV) ASCII, is available in the online journal. Below, we define all table columns.

- `mi_me` is the ion-electron mass ratio $m_{\rm i}/m_{\rm e}$.
- `theta` and `phi` specify the upstream magnetic field orientation, measured in the simulation frame. θ is the angle between $\boldsymbol{B}$ and the x-coordinate axis. φ is the angle between the y-z plane projection of

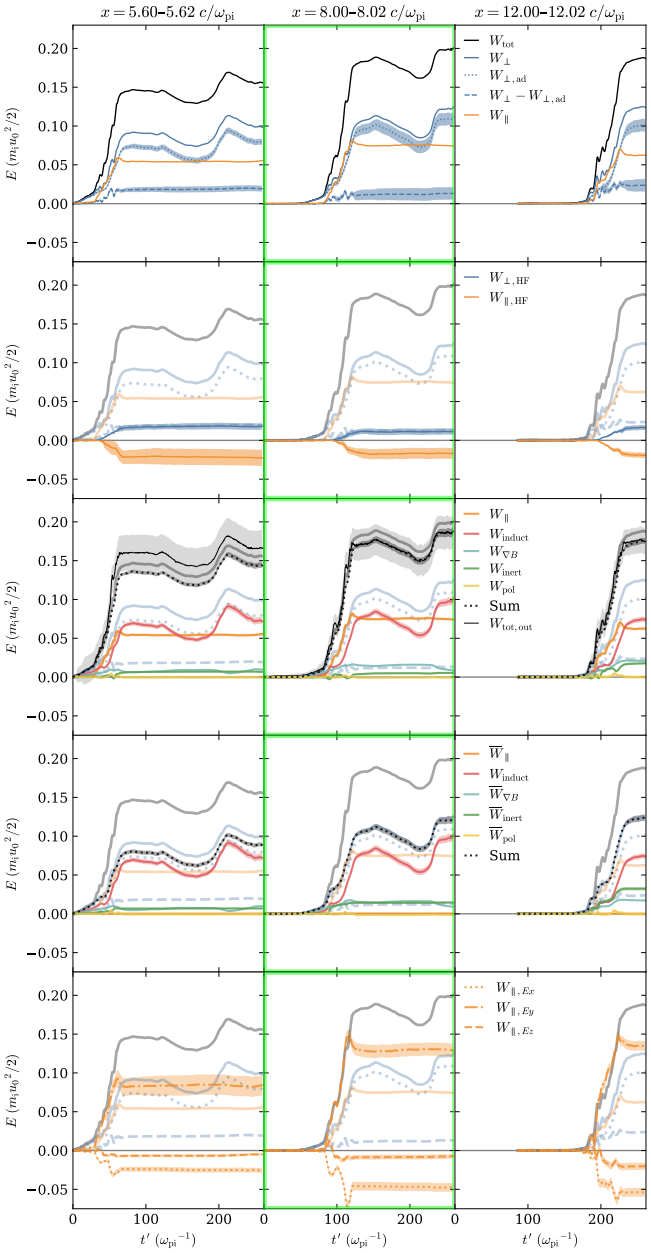


Figure 7. Like Fig. 4(a-b,e-g), but for multiple electron samples traversing the shock at different times. Left and right: first and last samples tracked. Middle (green box): sample shown in Figs. 3 and 4. Column titles indicate the sample's location at $t' = 0\ \omega_{\rm pi}{}^{-1}$. The complete figure (17 samples) is available in the online journal.

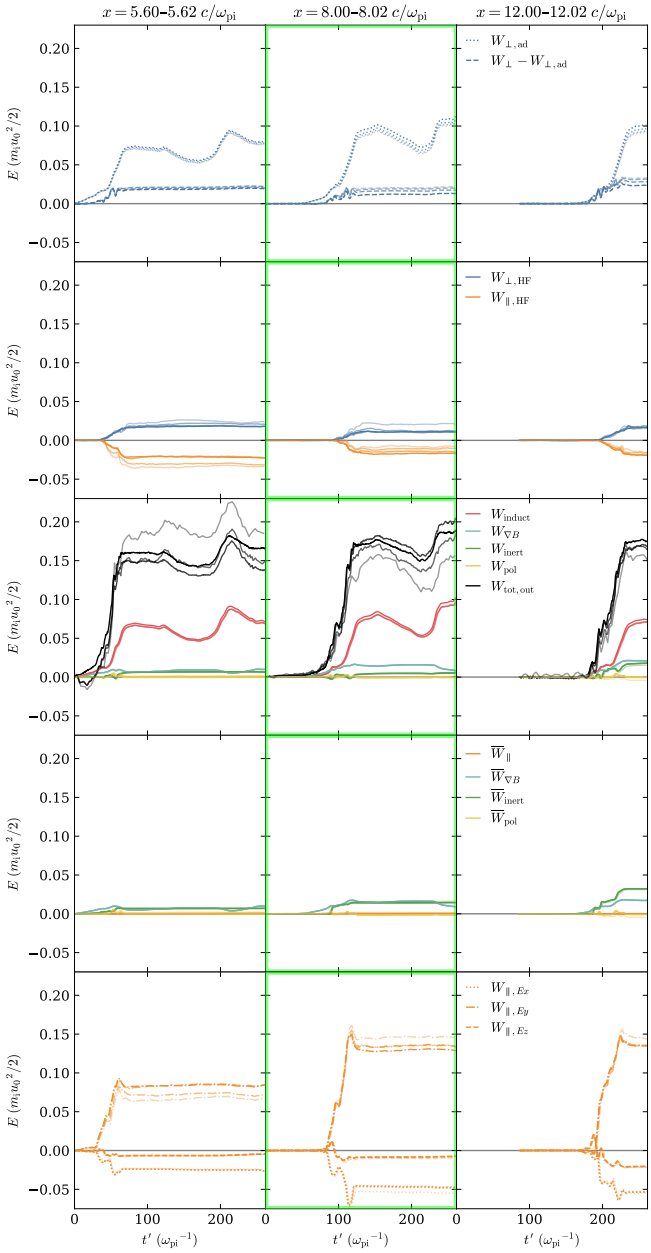


Figure 8. Like Fig. 7, but showing the numerical convergence of all quantities integrated with the coarse timestep $\Delta t_{\rm out}$, listed in text. For each quantity, we increase the sample spacing $\Delta t_{\rm out}$ by 2×, 4×, and 8× and plot the downsampled integration with progressively decreasing opacity. The complete figure (17 samples) is available in the online journal.

$\boldsymbol{B}$ and the z-coordinate axis. To visualize these angles, see Fig. 1 of Guo et al. (2014), but note that their $\varphi_{\rm B} = \pi/2 - \varphi$ is the complement of our φ. For all our simulations, θ corresponds to the angle between $\boldsymbol{B}$ and shock normal. The 2-D simulations with in-plane $\boldsymbol{B}$ have $\theta = 90°$ and $\varphi = 90°$. The 2-D simulations with out-of-plane $\boldsymbol{B}$ (i.e., $\boldsymbol{B}$ along $\hat{\boldsymbol{z}}$) have $\theta = 90°$ and $\varphi = 0°$. The 1-D simulations with oblique $\boldsymbol{B}$ have have $\theta < 90°$.

- `my` and `mz` are the numbers of grid cells along $\hat{\boldsymbol{y}}$ and $\hat{\boldsymbol{z}}$. Our 2-D simulations have `mz` $= 1$, and 1-D simulations have `my` $=$ `mz` $= 1$.

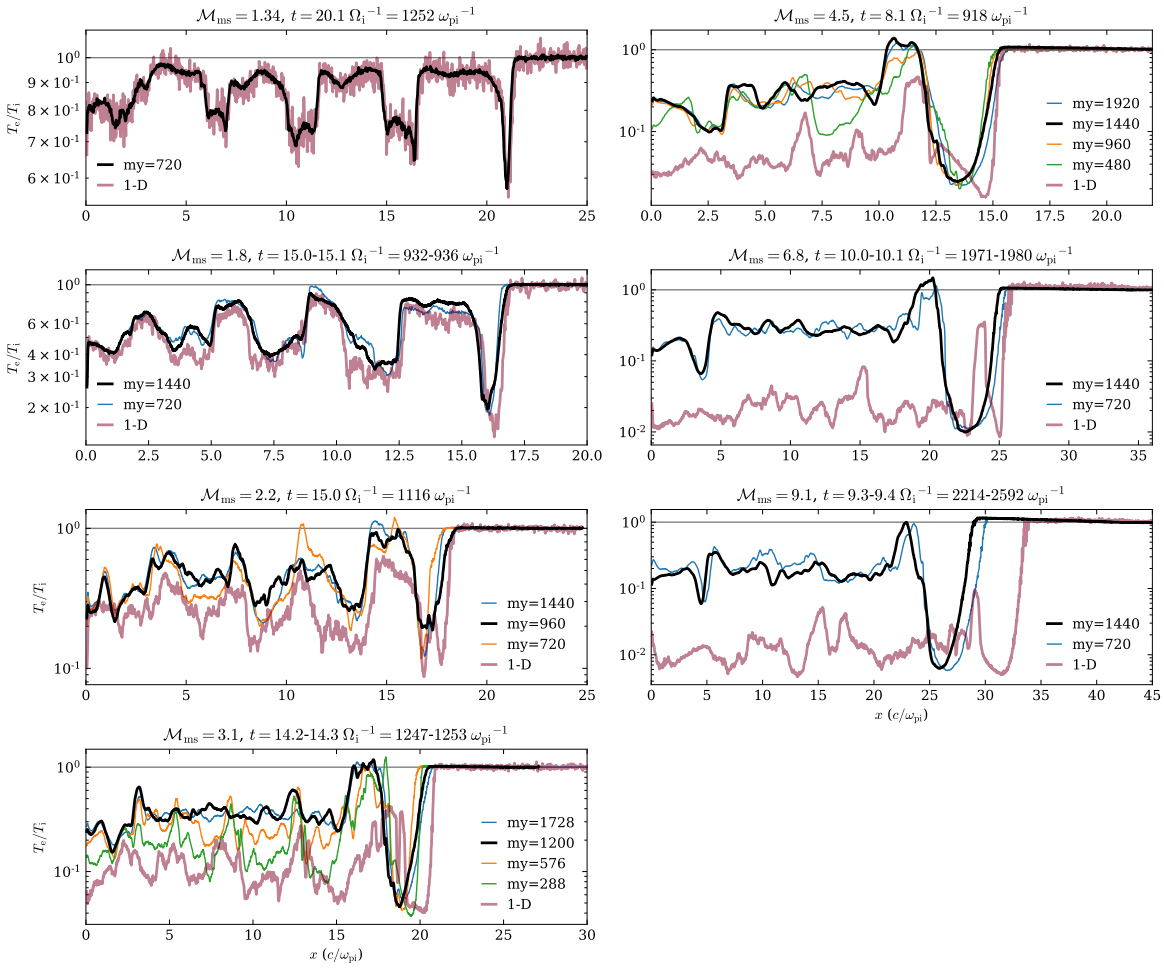


Figure 9. Fiducial 2-D simulations are converged with respect to transverse width. Black curves are fiducial 2-D $m_i/m_e = 625$, $\beta_p = 0.25$ simulations from Fig. 2(a). Colored curves are same shock parameters with varying input `my`, as defined in Table 1. A time range is given because simulation output times do not match exactly.

- `betap`, `Ms`, `Ma`, and `Mms` are the shock plasma beta β_p, sonic Mach number $\mathcal{M}_s$, Alfvén Mach number $\mathcal{M}_A$, and fast magnetosonic Mach number $\mathcal{M}_{ms}$. These numbers are *derived* from TRISTAN-MP input parameters `sigma`, `delgam`, and `u0` (defined just below). First, the total plasma beta is:

$$\beta_p = \frac{4\gamma_0\Delta\gamma_i}{\sigma\,(\gamma_0 - 1)\,(1 + m_e/m_i)}$$

where $\gamma_0 = 1/\sqrt{1 - (u_0/c)^2}$ is the Lorentz factor of the upstream flow in the simulation frame. The sonic Mach number depends on the upstream plasma speed in the shock's rest frame:

$$\mathcal{M}_s = \frac{u_{sh}}{c_s} = \frac{u_0}{(1 - 1/r\,(\mathcal{M}_s))\,c_s}$$

and we solve this implicit expression for $\mathcal{M}_s$ (and thus also u_{sh}) using an input u_0 and assumed fluid adiabatic index $\Gamma = 2$ (note that Γ enters into both the Rankine-Hugoniot expression for MHD shock compression ratio r and the sound speed c_s). Once $\mathcal{M}_s$ and u_{sh} are known, $\mathcal{M}_A$ and $\mathcal{M}_{ms}$ are known as well. This procedure for estimating shock parameters is taken directly from Guo et al. (2017).

- `sigma` is the magnetization, a ratio of upstream magnetic and kinetic enthalpy densities:

$$\texttt{sigma} = \sigma \equiv \frac{{B_0}^2}{4\pi\,(\gamma_0 - 1)\,(m_i + m_e)\,n_0 c^2}.$$

- `delgam` is the upstream plasma temperature, scaled by ion rest energy:

$$\texttt{delgam} = \Delta\gamma_i \equiv \frac{k_B T_0}{m_i c^2}.$$

- `u0` is the upstream plasma velocity, scaled by speed of light:

$$\texttt{u0} \equiv u_0/c$$

- `ppc0` is number of particles (both electrons and ions) per cell in the upstream plasma.
- `c_omp` is the number of grid cells per electron skin depth $c/\omega_{\rm pe}$.
- `ntimes` is the number of current filter passes.
- `dur` is the simulation duration in units of upstream ion cyclotron time ${\Omega_{\rm i}}^{-1}$.
- `Te_Ti` is our measurement of downstream temperature ratio $T_{\rm e}/T_{\rm i}$. As described in the main text, we manually choose a downstream region that is minimally affected by the left-side reflecting wall and the right-side shock front relaxation. Our measurement of $T_{\rm e}/T_{\rm i}$ uses downsampled grid output of the particle temperature tensor; however, the temperature tensor itself is calculated for each grid cell using the full particle distribution in a 5^N cell region, where $N \in \{1, 2, 3\}$ is the domain dimensionality.
- `Te_Ti_std` is the standard deviation of $T_{\rm e}/T_{\rm i}$ within the downstream region that we consider. Like `Te_Ti`, downsampled grid output is used for this estimate.
- `Te` and `Ti` are the downstream electron and ion temperatures scaled to their respective rest masses; i.e., $k_{\rm B}T_{\rm e}/(m_{\rm e}c^2)$ and $k_{\rm B}T_{\rm i}/(m_{\rm i}c^2)$. We measure all of `Te`, `Ti`, and `Te_Ti` in the same manually-chosen downstream region.

Table 1. Simulation input parameters, derived shock parameters, run duration, and downstream temperature measurements. Columns are defined in Appendix D.

mi_me	theta	phi	my	mz	betap	Ms	Ma	Mms	sigma	delgam	u0	ppc0	c_omp	ntimes	dur	Te_Ti	Te_Ti_std	Te	Ti
625	90	90	2400	1	0.250	6.86	3.43	3.07	4.7854E−1	8.0944E−6	2.3245E−2	128	20	64	6.7	...	...	...	...
625	90	90	720	1	0.251	3.00	1.50	1.34	1.0117E+1	1.6189E−5	7.1502E−3	32	10	32	20.1	8.53E−1	1.38E−1	1.29E−2	2.43E−5
625	90	90	1440	1	0.250	4.00	2.00	1.79	2.3774E+0	1.6189E−5	1.4749E−2	32	10	32	15.0	5.59E−1	2.33E−1	1.74E−2	4.96E−5
625	90	90	960	1	0.250	5.00	2.50	2.24	1.1237E+0	1.1332E−5	1.7949E−2	32	10	32	20.1	4.52E−1	1.69E−1	1.96E−2	6.92E−5
625	90	90	1200	1	0.250	6.86	3.43	3.07	4.7854E−1	8.0944E−6	2.3245E−2	32	10	32	14.2	3.65E−1	1.28E−1	2.83E−2	1.24E−4
625	90	90	1440	1	0.250	9.99	4.99	4.47	1.9968E−1	4.8566E−6	2.7873E−2	32	10	32	12.1	3.18E−1	1.22E−1	3.65E−2	1.83E−4
625	90	90	1440	1	0.250	15.19	7.60	6.79	8.1402E−2	1.6189E−6	2.5205E−2	32	10	32	10.0	2.97E−1	1.22E−1	2.80E−2	1.51E−4
625	90	90	1440	1	0.250	20.37	10.18	9.11	4.4398E−2	8.0944E−7	2.4133E−2	32	10	32	9.8	1.98E−1	5.99E−2	1.83E−2	1.47E−4
625	90	0	1440	1	0.251	3.00	1.50	1.34	1.0117E+1	1.6189E−5	7.1502E−3	32	10	32	19.0	8.62E−1	1.20E−1	1.30E−2	2.42E−5
625	90	0	1440	1	0.250	4.00	2.00	1.79	2.3774E+0	1.6189E−5	1.4749E−2	32	10	32	19.9	4.71E−1	1.78E−1	1.60E−2	5.42E−5
625	90	0	1440	1	0.250	5.00	2.50	2.24	1.1237E+0	1.1332E−5	1.7949E−2	32	10	32	15.0	2.49E−1	1.28E−1	1.24E−2	7.93E−5
625	90	0	1440	1	0.250	7.00	3.50	3.13	4.5493E−1	8.0944E−6	2.3840E−2	32	10	32	15.2	1.07E−1	5.45E−2	1.02E−2	1.54E−4
625	90	0	1440	1	0.250	10.00	5.00	4.47	1.9912E−1	4.8566E−6	2.7912E−2	32	10	32	9.8	4.48E−2	2.30E−2	6.82E−3	2.44E−4
625	90	0	1440	1	0.250	15.00	7.50	6.71	8.3580E−2	1.6189E−6	2.4874E−2	32	10	32	8.5	2.54E−2	2.43E−2	3.11E−3	1.96E−4
625	90	90	1	1	0.251	3.00	1.50	1.34	1.0117E+1	1.6189E−5	7.1502E−3	512	10	32	40.0	8.52E−1	1.05E−1	1.32E−2	2.47E−5
625	90	90	1	1	0.250	4.00	2.00	1.79	2.3774E+0	1.6189E−5	1.4749E−2	512	10	32	40.0	4.28E−1	1.86E−1	1.58E−2	5.92E−5
625	90	90	1	1	0.250	5.00	2.50	2.24	1.1237E+0	1.1332E−5	1.7949E−2	512	10	32	25.2	2.36E−1	8.40E−2	1.24E−2	8.40E−5
625	90	90	1	1	0.250	7.00	3.50	3.13	4.5493E−1	8.0944E−6	2.3840E−2	512	10	32	25.0	1.01E−1	3.87E−2	1.02E−2	1.61E−4
625	90	90	1	1	0.250	10.00	5.00	4.47	1.9912E−1	4.8566E−6	2.7912E−2	512	10	32	15.2	5.02E−2	3.44E−2	7.03E−3	2.24E−4
625	90	90	1	1	0.250	15.00	7.50	6.71	8.3580E−2	1.6189E−6	2.4874E−2	1024	10	32	15.1	2.38E−2	1.57E−2	2.85E−3	1.92E−4
625	90	90	1	1	0.250	20.00	10.00	8.94	4.6080E−2	1.1332E−6	2.8027E−2	2048	10	32	10.1	1.35E−2	1.18E−2	2.05E−3	2.43E−4
625	85	90	1	1	0.251	3.00	1.50	1.34	1.0117E+1	1.6189E−5	7.1502E−3	2048	10	64	40.0	9.15E−1	7.96E−2	1.36E−2	2.38E−5
625	85	90	1	1	0.250	4.00	2.00	1.79	2.3774E+0	1.6189E−5	1.4749E−2	2048	10	64	40.0	4.91E−1	1.61E−1	1.70E−2	5.54E−5
625	85	90	1	1	0.250	5.00	2.50	2.23	1.1237E+0	1.1332E−5	1.7949E−2	2048	10	64	25.2	2.79E−1	1.57E−1	1.36E−2	7.79E−5
625	85	90	1	1	0.250	7.00	3.50	3.13	4.5493E−1	8.0944E−6	2.3840E−2	2048	10	64	20.0	1.35E−1	4.98E−2	1.35E−2	1.60E−4
625	85	90	1	1	0.250	10.00	5.00	4.47	1.9912E−1	4.8566E−6	2.7912E−2	2048	10	64	15.2	1.29E−1	3.69E−2	1.75E−2	2.17E−4
625	80	90	1	1	0.251	2.99	1.50	1.34	1.0117E+1	1.6189E−5	7.1502E−3	2048	10	64	30.1	8.73E−1	4.51E−2	1.27E−2	2.32E−5
625	80	90	1	1	0.250	3.99	2.00	1.79	2.3774E+0	1.6189E−5	1.4749E−2	2048	10	64	30.1	6.58E−1	1.09E−1	1.94E−2	4.72E−5
625	80	90	1	1	0.250	4.99	2.50	2.23	1.1237E+0	1.1332E−5	1.7949E−2	2048	10	64	25.2	5.28E−1	1.62E−1	2.13E−2	6.45E−5
625	80	90	1	1	0.250	6.99	3.49	3.13	4.5493E−1	8.0944E−6	2.3840E−2	2048	10	64	20.0	2.38E−1	1.27E−1	2.05E−2	1.38E−4
625	80	90	1	1	0.250	9.99	5.00	4.47	1.9912E−1	4.8566E−6	2.7912E−2	2048	10	64	15.2	1.89E−1	8.87E−2	2.27E−2	1.91E−4
625	75	90	1	1	0.251	2.98	1.49	1.34	1.0117E+1	1.6189E−5	7.1502E−3	2048	10	64	40.0	8.54E−1	2.44E−2	1.27E−2	2.37E−5
625	75	90	1	1	0.250	3.98	1.99	1.78	2.3774E+0	1.6189E−5	1.4749E−2	2048	10	64	30.1	6.45E−1	7.82E−2	1.94E−2	4.80E−5
625	75	90	1	1	0.250	4.98	2.49	2.23	1.1237E+0	1.1332E−5	1.7949E−2	2048	10	64	25.2	7.76E−1	1.81E−1	2.69E−2	5.55E−5
625	75	90	1	1	0.250	6.98	3.49	3.12	4.5493E−1	8.0944E−6	2.3840E−2	2048	10	64	20.0	1.11E+0	1.90E−1	5.52E−2	7.95E−5
625	75	90	1	1	0.250	9.98	4.99	4.46	1.9912E−1	4.8566E−6	2.7912E−2	2048	10	64	15.2	2.58E−1	1.27E−1	3.09E−2	1.92E−4
20	90	90	720	1	0.250	3.00	1.50	1.34	9.8755E+0	5.0590E−4	3.9505E−2	32	10	32	39.2	8.62E−1	9.55E−2	1.29E−2	7.46E−4
20	90	90	720	1	0.250	4.00	2.00	1.79	2.2975E+0	5.0590E−4	8.1851E−2	32	10	32	39.2	4.43E−1	1.69E−1	1.58E−2	1.79E−3

Table 1 *continued*

Table 1 *(continued)*

mi_me	theta	phi	my	mz	betap	Ms	Ma	Mms	sigma	delgam	u0	ppc0	c_omp	ntimes	dur	Te_Ti	Te_Ti_std	Te	Ti
20	90	90	720	1	0.250	5.00	2.50	2.24	1.0872E+0	3.5413E−4	9.9512E−2	32	10	32	29.5	2.83E−1	1.40E−1	1.38E−2	2.44E−3
20	90	90	720	1	0.250	6.84	3.42	3.06	4.6363E−1	2.5295E−4	1.2868E−1	32	10	32	24.5	2.13E−1	8.37E−2	1.73E−2	4.07E−3
20	90	90	720	1	0.250	9.93	4.97	4.44	1.9289E−1	1.5177E−4	1.5439E−1	32	10	32	19.6	1.85E−1	8.66E−2	2.34E−2	6.33E−3
20	90	90	720	1	0.250	15.12	7.56	6.76	7.9463E−2	5.0590E−5	1.3896E−1	32	10	32	14.7	1.70E−1	4.14E−2	1.82E−2	5.36E−3
20	90	90	960	1	0.250	20.27	10.14	9.07	4.3483E−2	2.5295E−5	1.3285E−1	32	10	32	14.7	1.64E−1	4.36E−2	1.69E−2	5.15E−3
49	90	90	1440	1	0.250	3.00	1.50	1.34	1.0020E+1	2.0649E−4	2.5420E−2	32	10	32	39.5	8.53E−1	1.09E−1	1.28E−2	3.07E−4
49	90	90	1440	1	0.250	4.00	2.00	1.79	2.3453E+0	2.0649E−4	5.2528E−2	32	10	32	39.5	4.78E−1	2.11E−1	1.59E−2	6.78E−4
49	90	90	1440	1	0.250	5.00	2.50	2.24	1.1090E+0	1.4454E−4	6.3899E−2	32	10	32	25.0	3.37E−1	1.71E−1	1.54E−2	9.32E−4
49	90	90	1440	1	0.250	6.85	3.42	3.06	4.7256E−1	1.0325E−4	8.2703E−2	32	10	32	25.6	3.26E−1	1.43E−1	2.35E−2	1.47E−3
49	90	90	1440	1	0.250	9.97	4.98	4.46	1.9696E−1	6.1947E−5	9.9192E−2	32	10	32	25.0	2.75E−1	6.97E−2	3.22E−2	2.39E−3
49	90	90	720	1	0.250	15.16	7.58	6.78	8.0625E−2	2.0649E−5	8.9530E−2	128	10	32	15.0	1.81E−1	4.46E−2	1.92E−2	2.16E−3
49	90	90	720	1	0.250	20.33	10.17	9.09	4.4032E−2	1.0325E−5	8.5672E−2	128	10	32	14.9	1.32E−1	3.76E−2	1.42E−2	2.19E−3
49	90	90	360	1	0.250	30.63	15.32	13.70	1.9157E−2	4.1298E−6	8.2153E−2	128	10	32	10.0	1.14E−1	3.67E−2	1.11E−2	1.97E−3
200	90	90	1440	1	0.250	3.00	1.50	1.34	1.0099E+1	5.0590E−5	1.2629E−2	32	10	32	33.1	8.54E−1	1.16E−1	1.28E−2	7.49E−5
200	90	90	1440	1	0.250	4.00	2.00	1.79	2.3715E+0	5.0590E−5	2.6060E−2	32	10	32	39.3	5.40E−1	2.04E−1	1.80E−2	1.66E−4
200	90	90	1440	1	0.250	5.00	2.50	2.24	1.1210E+0	3.5413E−5	3.1711E−2	32	10	32	29.0	4.75E−1	2.00E−1	2.03E−2	2.14E−4
200	90	90	1440	1	0.250	6.86	3.43	3.07	4.7744E−1	2.5295E−5	4.1064E−2	32	10	32	21.5	3.66E−1	1.52E−1	2.67E−2	3.65E−4
200	90	90	1440	1	0.250	9.98	4.99	4.46	1.9918E−1	1.5177E−5	4.9241E−2	32	10	32	20.0	3.73E−1	1.16E−1	3.91E−2	5.24E−4
200	90	90	1440	1	0.250	15.18	7.59	6.79	8.1259E−2	5.0590E−6	4.4512E−2	32	10	32	15.0	2.44E−1	7.44E−2	2.51E−2	5.14E−4
200	90	90	1440	1	0.250	20.36	10.18	9.11	4.4331E−2	2.5295E−6	4.2614E−2	64	10	32	10.2	1.51E−1	6.25E−2	1.55E−2	5.13E−4
49	90	90	192	192	0.250	4.00	2.00	1.79	2.3453E+0	2.0649E−4	5.2528E−2	32	10	32	24.1	4.65E−1	2.23E−1	1.57E−2	6.90E−4
49	90	90	192	192	0.250	5.00	2.50	2.24	1.1090E+0	1.4454E−4	6.3899E−2	32	10	32	35.3	3.37E−1	2.07E−1	1.57E−2	9.54E−4
49	90	90	192	384	0.250	6.85	3.42	3.06	4.7256E−1	1.0325E−4	8.2703E−2	32	10	32	17.4	2.74E−1	1.40E−1	2.12E−2	1.58E−3
49	90	90	192	192	0.250	9.97	4.98	4.46	1.9696E−1	6.1947E−5	9.9192E−2	32	10	32	15.0	2.37E−1	1.61E−1	2.84E−2	2.45E−3
49	90	90	192	192	0.250	15.16	7.58	6.78	8.0625E−2	2.0649E−5	8.9530E−2	32	10	32	8.9	1.50E−1	7.62E−2	1.58E−2	2.16E−3
49	90	90	1440	1	0.125	4.00	1.41	1.33	1.1537E+1	2.0649E−4	3.3500E−2	32	10	32	24.8	7.71E−1	1.32E−1	1.28E−2	3.38E−4
49	90	90	1440	1	0.125	5.00	1.77	1.67	3.4565E+0	1.4454E−4	5.1197E−2	32	10	32	24.8	4.14E−1	1.98E−1	1.06E−2	5.22E−4
49	90	90	1440	1	0.125	6.68	2.36	2.23	1.2431E+0	1.0325E−4	7.2128E−2	32	10	32	25.0	2.42E−1	1.35E−1	1.14E−2	9.66E−4
49	90	90	1440	1	0.125	9.78	3.46	3.26	4.4927E−1	6.1947E−5	9.2894E−2	32	10	32	24.8	3.09E−1	1.34E−1	2.68E−2	1.77E−3
49	90	90	1440	1	0.125	14.99	5.30	5.00	1.7122E−1	2.0649E−5	8.6888E−2	32	10	32	20.1	2.65E−1	8.51E−2	2.32E−2	1.79E−3
49	90	90	1440	1	0.125	20.19	7.14	6.73	9.1148E−2	1.0325E−5	8.4213E−2	32	10	32	15.1	2.10E−1	6.01E−2	1.88E−2	1.83E−3
49	90	90	360	1	0.125	30.53	10.79	10.18	3.8916E−2	4.1298E−6	8.1516E−2	128	10	32	10.1	1.47E−1	8.28E−2	1.36E−2	1.89E−3
49	90	90	720	1	0.500	2.00	1.41	1.15	3.5805E+1	2.0649E−4	9.5092E−3	32	10	32	38.8	9.95E−1	6.62E−2	1.14E−2	2.34E−4
49	90	90	1440	1	0.500	3.00	2.12	1.73	2.2310E+0	2.0649E−4	3.8088E−2	32	10	32	38.8	6.17E−1	1.70E−1	1.54E−2	5.09E−4
49	90	90	1440	1	0.500	3.87	2.74	2.24	9.2639E−1	2.0649E−4	5.9093E−2	32	10	32	25.9	3.99E−1	1.41E−1	1.93E−2	9.85E−4
49	90	90	1440	1	0.500	4.90	3.47	2.83	4.8236E−1	1.4454E−4	6.8506E−2	32	10	32	26.0	4.00E−1	1.29E−1	2.30E−2	1.17E−3
49	90	90	1440	1	0.500	6.98	4.93	4.03	2.0639E−1	1.0325E−4	8.8477E−2	32	10	32	25.6	2.80E−1	5.22E−2	2.81E−2	2.04E−3
49	90	90	1440	1	0.500	10.08	7.13	5.82	9.2084E−2	6.1947E−5	1.0257E−1	32	10	32	25.5	2.05E−1	3.55E−2	2.94E−2	2.94E−3
49	90	90	1440	1	0.500	15.26	10.79	8.81	3.9095E−2	2.0649E−5	9.0910E−2	32	10	32	19.9	1.47E−1	1.99E−2	1.78E−2	2.47E−3
49	90	90	1440	1	1.000	2.00	2.00	1.41	4.4802E+0	2.0649E−4	1.9008E−2	32	10	32	25.0	9.19E−1	1.39E−1	1.34E−2	2.97E−4

Table 1 *continued*

Table 1 *(continued)*

mi_me	theta	phi	my	mz	betap	Ms	Ma	Mms	sigma	delgam	u0	ppc0	c_omp	ntimes	dur	Te_Ti	Te_Ti_std	Te	Ti
49	90	90	1440	1	1.000	3.00	3.00	2.12	8.2034E−1	2.0649E−4	4.4412E−2	32	10	32	25.0	5.18E−1	1.55E−1	1.76E−2	6.95E−4
49	90	90	1440	1	1.000	4.00	4.00	2.83	3.6299E−1	2.0649E−4	6.6745E−2	32	10	32	25.0	3.64E−1	1.08E−1	2.37E−2	1.33E−3
49	90	90	1440	1	1.000	4.99	4.99	3.53	2.1083E−1	1.4454E−4	7.3265E−2	32	10	32	24.8	3.42E−1	8.28E−2	2.55E−2	1.52E−3
49	90	90	1440	1	1.000	7.06	7.06	4.99	9.6333E−2	1.0325E−4	9.1569E−2	32	10	32	24.8	2.18E−1	3.84E−2	2.54E−2	2.37E−3
49	90	90	1440	1	1.000	10.15	10.15	7.18	4.4490E−2	6.1947E−5	1.0434E−1	32	10	32	25.0	1.59E−1	2.53E−2	2.49E−2	3.19E−3
49	90	90	1440	1	1.000	15.31	15.31	10.82	1.9246E−2	2.0649E−5	9.1619E−2	32	10	32	24.8	1.32E−1	1.91E−2	1.64E−2	2.53E−3
49	90	90	1440	1	2.000	2.00	2.83	1.63	1.4344E+0	2.0649E−4	2.3754E−2	32	10	32	24.8	8.56E−1	1.86E−1	1.50E−2	3.58E−4
49	90	90	1440	1	2.000	3.00	4.24	2.45	3.5747E−1	2.0649E−4	4.7572E−2	32	10	32	24.8	5.24E−1	9.73E−2	2.04E−2	7.93E−4
49	90	90	1512	1	2.000	4.00	5.66	3.27	1.6927E−1	2.0649E−4	6.9110E−2	32	10	32	27.8	3.39E−1	4.34E−2	2.63E−2	1.59E−3
49	90	90	1512	1	2.000	5.00	7.07	4.08	1.0012E−1	2.0649E−4	8.9824E−2	32	10	32	24.6	2.58E−1	3.86E−2	3.21E−2	2.55E−3
49	90	90	1440	1	2.000	7.11	10.05	5.80	4.6506E−2	1.0325E−4	9.3186E−2	32	10	32	24.9	1.86E−1	2.32E−2	2.42E−2	2.66E−3
49	90	90	2016	1	2.000	10.19	14.41	8.32	2.1861E−2	6.1947E−5	1.0525E−1	32	10	32	18.8	1.33E−1	1.29E−2	2.26E−2	3.46E−3
49	90	90	1440	1	2.000	15.33	21.69	12.52	9.5477E−3	2.0649E−5	9.1978E−2	32	10	32	12.0	1.22E−1	2.36E−2	1.57E−2	2.63E−3
49	90	90	1440	1	4.000	2.00	4.00	1.79	5.9285E−1	2.0649E−4	2.6126E−2	32	10	32	25.1	8.35E−1	1.87E−1	1.62E−2	3.96E−4
49	90	90	1512	1	4.000	3.00	6.00	2.68	1.6743E−1	2.0649E−4	4.9151E−2	32	10	32	23.8	4.90E−1	6.76E−2	2.21E−2	9.19E−4
49	90	90	1512	1	4.000	4.00	8.00	3.58	8.1810E−2	2.0649E−4	7.0292E−2	32	10	32	34.3	3.45E−1	4.17E−2	2.79E−2	1.65E−3
49	90	90	1512	1	4.000	5.00	10.00	4.47	4.9023E−2	2.0649E−4	9.0767E−2	32	10	32	36.6	2.60E−1	2.30E−2	3.32E−2	2.61E−3
49	90	90	1440	1	4.000	7.13	14.27	6.38	2.2843E−2	1.0325E−4	9.4017E−2	32	10	32	25.1	1.69E−1	1.46E−2	2.31E−2	2.79E−3
49	90	90	2160	1	4.000	10.21	20.42	9.13	1.0835E−2	6.1947E−5	1.0571E−1	32	10	32	19.0	1.35E−1	1.22E−2	2.33E−2	3.52E−3

NOTE— Table 1 is available in a machine-readable CSV format in the online journal.